Icarus 331 (2019) 116–126

Contents lists available at ScienceDirect

Icarus

journal homepage: www.elsevier.com/locate/icarus

A reanalysis of the relationship between the size of boulders and craters in lunar surface

Mengna Jia[a,b], Zongyu Yue[a,e,*], Kaichang Di[a,c,e], Bin Liu[a], Jianzhong Liu[d,e]

[a] State Key Laboratory of Remote Sensing Science, Institute of Remote Sensing and Digital Earth Chinese Academy of Sciences, Beijing 100101, China
[b] University of Chinese Academy of Sciences, Beijing 100049, China
[c] State Key Laboratory of Lunar and Planetary Sciences, Macau University of Science and Technology, Macau 999078, China
[d] Institute of Geochemistry Chinese Academy of Sciences, Guiyang 550002, China
[e] CAS Center for Excellence in Comparative Planetology, Hefei, 230026, China

ARTICLE INFO

Keywords:
Boulders
Craters
Lunar

ABSTRACT

To distinguish secondary craters from primary craters is very important in lunar studies that involve such tasks as dating the lunar surface and investigating the meteoritic flux. However, this is usually difficult since distant secondary craters generally have an appearance similar to primary ones. Bart and Melosh (2007a, 2007b) proposed a method to distinguish the two types of craters based on the relationship between the crater diameter (D) and the size of the largest boulder (B) around the crater: $B = KD^{2/3}$, where K is the fitting coefficient. They concluded that secondary craters have a 60% larger fitting coefficient (K) than primary craters. However, because of the poor quality of the available data and an insufficient number of crater samples, their results need further substantiation, as they have suggested. This research aims to examine their results with recently obtained very high resolution data and many more sampled craters. Our results indicate that the criterion proposed by Bart and Melosh (2007a, 2007b) is actually not applicable, i.e., the fitted coefficient (K), in cases of primary and secondary craters, cannot be confidently distinguished.

1. Introduction

Lunar surface dating is a fundamental and important task in lunar geologic study, and one of the most popular methods is to analyze the density of craters in the surveyed area (e.g., Shoemaker et al., 1962; van der Bogert et al., 2010; Hiesinger et al., 2012; Orgel et al., 2018). During this process, only primary craters should be counted, in consideration of their random distribution in space (Michael et al., 2012, 2016). Secondary craters should be excluded in lunar surface dating because huge numbers of them form nearly simultaneously such that two surfaces of equal age may differ by several orders of magnitude (McEwen and Bierhaus, 2006). In addition, secondary craters are closely related to the ejection process, which is one of the dominant processes responsible for the transport of lunar boulders (Bart and Melosh, 2010), the formation and evolution of the lunar regolith (Wilcox et al., 2005), and even the formation of lunar meteorites (Head et al., 2002). Finally, the identification of secondary craters is also important in inversing the meteoritic flux (Melosh, 1989, Page 187), which is of great importance in the study of the impact environment.

In general, lunar secondary craters are distributed as chains around their primary crater and are characterized by their irregular shape, shallow depth, and herringbone ejecta pattern (e.g., Shoemaker et al., 1962; Oberbeck and Morrison, 1973). However, for distant secondary craters, they are more circular in outline and are more widely dispersed, resembling similarly sized primary craters in the background (Wilhelms et al., 1978; McEwen and Bierhaus, 2006; Kumar et al., 2011) because the impact velocities that create them greatly increase with distance (Ahrens and O'Keefe, 1978; Melosh, 1989). As a result, isolated distant secondary craters can be misinterpreted as primary craters. Thus, distinguishing them from primary ones in related applications merits attention. Bart and Melosh (2007a) proposed a method using the size distribution of boulders around impact craters to distinguish distant secondary craters from the same-sized primary craters. They established an empirical equation between the sizes of boulders and impact craters, and they pointed out that the fitted coefficient for the secondary crater is 60% larger than that of the primary crater (Bart and Melosh, 2007a). This method sheds light on the solution to this perplexing problem. However, only 18 crater samples, including six secondary craters, were considered in their study. In addition, the data they employed were photographic films from Lunar Orbiter III, V, and

* Corresponding author at: P. O. Box 9718, Datun Road, Chaoyang District, Beijing 100101, China.
E-mail address: yuezy@radi.ac.cn (Z. Yue).

https://doi.org/10.1016/j.icarus.2019.05.009
Received 30 September 2018; Received in revised form 4 April 2019; Accepted 7 May 2019
Available online 09 May 2019
0019-1035/

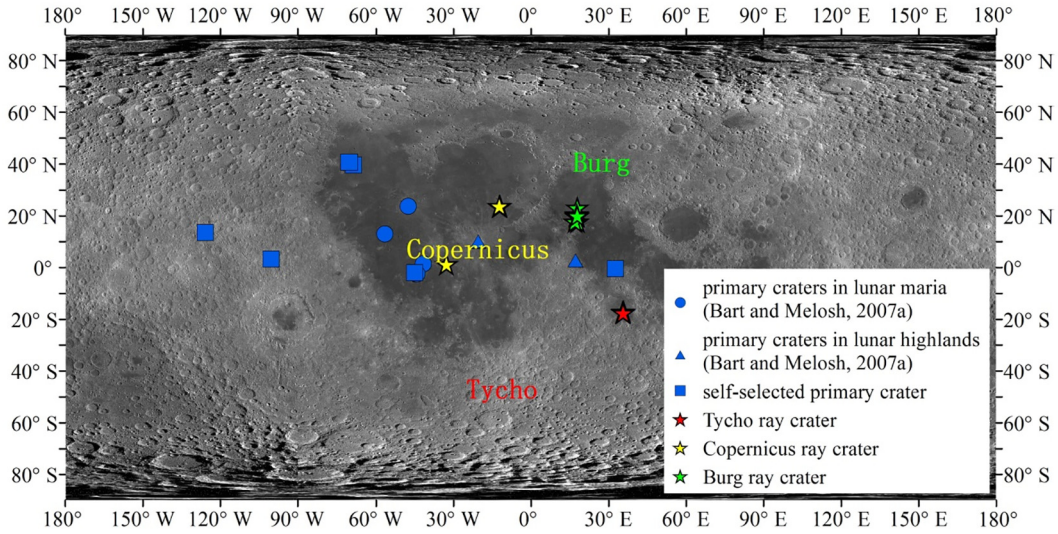

Fig. 1. Locations for selected crater samples. Distant secondary craters are indicated by stars with different colors showing different sources, and the names of the corresponding primary craters are also displayed. Primary craters are indicated in blue with different shapes showing different sources. The "primary craters in lunar maria" and "primary craters in lunar highlands" are primary craters involved in Bart and Melosh (2007a). The "self-selected primary crater" is the primary crater that is selected in this study and not used by Bart and Melosh (2007a). The basemap is a LROC WAC global mosaic product (Speyerer et al., 2011; Wagner et al., 2015). (For interpretation of the references to colour in this figure legend, the reader is referred to the web version of this article.)

Apollo 17, which have poor quality in related measurements and boulder identification. Thus, as they admitted in their study, their conclusion requires further verification with high resolution and high quality images as well as more crater samples. Recently, there have been many more very high resolution lunar images obtained, which provides the opportunity to verify their conclusions, and this is precisely the objective of this research.

In this study, we used images from the Lunar Reconnaissance Orbiter Camera (LROC) Narrow-Angle Camera (NAC), the highest resolution images to date. The up to sub-meter resolution makes it possible to identify several-meter-scale boulders, which is a positive relief with the presence of an elongated shadow and appears detached from the ground where it stands (Pajola et al., 2018), facilitating the reanalysis of the relationship between the largest boulder size and the corresponding crater diameter. We selected 41 sample craters, including 16 craters from Bart and Melosh (2007a, 2007b), to provide a reliable analysis on this subject. The results demonstrate that the largest boulder size is positively correlated with crater diameter. There is no significant difference between the coefficients of the two types of craters, so the methods of Bart and Melosh (2007a) are unable to distinguish distant secondary craters from primary craters.

2. Data and method

2.1. LROC images

The LRO mission was launched in June 18, 2009, and NAC is a pair camera that provides high resolution images (Robinson et al., 2010). The data products from LROC NAC can be downloaded from the Planetary Data System website and were subsequently processed with the software of Integrated System for Imagers and Spectrometers (Anderson et al., 2014). In this research, the data products of the Experimental Data Record level were used, which were processed by attaching the SPICE kernels (NAIF, 2014) with "spiceinit", performing radiometric corrections with "lronaccal", removing the echo effects with "lronacecho", and applying a map projection with "cam2map" in sequence. The influence of each processing step on the NAC image can be found in the supplementary document. In the end, a data product that can be used to identify and measure craters and boulders is produced. To remove the influence of shadows, up to several images were used from the same location to find the one that has the least illumination influence and gives the largest boulder size measurement. As a result, more than 200 images were used, with resolutions ranging from 0.4 m/pixel to 2.3 m/pixel. The illumination condition and the resolution of the involved images are listed in Table S2 of the supplementary file.

The Wide Angle Camera (WAC) is another payload in the LRO spacecraft, which is a push-frame camera with resolutions of 75 and 384 m (at an altitude of 50 km) in the visible and ultraviolet bands, respectively (Robinson et al., 2010). LROC WAC covers a swath ~104 km wide from the nominal 50-km orbit (Robinson et al., 2010), which allowed the instrument team to create a global mosaic with high quality. In this research, a WAC global mosaic created in June 2013 (https://astrogeology.usgs.gov/search/map/Moon/LRO/LROC_WAC/Lunar_LRO_LROC-WAC_Mosaic_global_100m_June2013) was used as the basemap (Speyerer et al., 2011; Sato et al., 2014; Wagner et al., 2015).

2.2. Sampled craters and measurements

There are 18 craters involved in Bart and Melosh (2007a, 2007b), including six distant secondary craters associated with the Burg crater ray, six primary craters in the highlands and six primary craters in the lunar maria. Sixteen of these craters were included in this study, except two primary craters in the highlands (V-167-H2(b) and V-167-H3 in Bart and Melosh (2007a, 2007b)), which fail to be found in the NAC images. We also selected seven other distant secondary craters associated with the Burg ray according to the identification principle used by Bart and Melosh (2007a), i.e., they have apparent similar ages (e.g. similar visual degradation condition (Fassett et al., 2012; Fassett and Thomson, 2014)), and they are in proximity to one another in addition to residing in the ray of Burg crater. Three distant secondary craters associated with Copernicus crater ray identified by Kumar et al. (2011) and another two craters in this area identified as distant secondary craters in this study were also included, according to the above principles. In addition, another seven distant secondary craters associated with Tycho crater ray, which were identified by Basilevsky et al. (2018), were also added for analysis in this research. As for the primary craters, craters of Censorinus and Pierazzo (McEwen, 2018), and another four unnamed small craters that have fresh appearance were included in this study. As a result, 25 distant secondary craters and 16

Table 1

The largest boulder size, mean size of the largest five boulders, the crater diameter and the center location of 41 crater samples used in this study. The crater ID begins with an 'S' for the distant secondary craters and a 'P' for the primary craters. S1–S6 and P1–P10 are the same as those in Bart and Melosh (2007a, 2007b), and the photograph numbers in the last column display the crater correspondence between the two studies. Identifications by Kumar et al. (2011) and Basilevsky et al. (2018) are also annotated, and the others are selected in this study. The measurement results from Bart and Melosh (2007a, 2007b) are also listed in italics for comparison. The measurement difference of crater diameter and boulder size between Bart and Melosh (2007a, 2007b)' and our results is also calculated and shown in the table. It is calculated with the equation: *Difference* = $(m_1 - m_2)/m_2$, where "m_1" represents the measurement from Bart and Melosh (2007a, 2007b) and "m_2" is the measurement from our research.

Crater ID	Largest boulder (m)			Mean of 5 largest (m)			Crater diameter (m)			Crater center longitude	Crater center latitude	Distance to the primary (km)	Note
	This study	Bart and Melosh (2007a, 2007b)	Difference (%)	This study	Bart and Melosh (2007a, 2007b)	Difference (%)	This study	Bart and Melosh (2007a, 2007b)	Difference (%)				
Burg crater ray													
S1	37.6	*57*	−34.04	28.7	*43*	−33.26	906.9	*1060*	−14.44	17.710	20.603	805.3	Ap17_2345(a)
S2	31.3	*44*	−28.86	26.3	*32*	−17.81	1143.6	*1300*	−12.03	17.770	20.560	805.9	Ap17_2345(b)
S3	35.4	*31*	14.19	30.7	*28*	9.64	1305.8	*1415*	−7.72	17.892	20.099	817.3	Ap17_2345(e)
S4	36.9	*41*	−10.0	30.0	*38*	−21.05	662.9	*730*	−9.19	17.919	19.986	820.1	Ap17_2345(f)
S5	27.0	*44*	−38.64	23.0	*34*	−32.35	615.2	*674*	−8.72	17.921	19.893	822.7	Ap17_2345(g)
S6	24.3	*47*	−48.30	22.5	*33*	−31.82	554.3	*591*	−6.21	17.493	19.801	830.2	Ap17_2345(i)
S7	31.4	/	/	29.0	/	/	773.8	/	/	17.450	20.543	810.1	This study
S8	21.5	/	/	18.3	/	/	456.1	/	/	17.473	20.184	821.6	
S9	18.9	/	/	17.1	/	/	367.8	/	/	17.558	20.210	818.0	
S10	13.4	/	/	9.7	/	/	171.7	/	/	17.954	23.113	732.8	
S11	10.1	/	/	7.9	/	/	173.8	/	/	17.080	17.772	891.8	
S12	30.0	/	/	22.9	/	/	615.2	/	/	18.023	17.729	882.7	
S13	13.1	/	/	11.2	/	/	328.5	/	/	17.032	17.768	892.5	
Copernicus crater ray													
S14	23.2	/	/	21.2	/	/	727.0	/	/	−12.269	23.553	484.3	Kumar et al., 2011
S15	23.6	/	/	21.1	/	/	719.2	/	/	−11.913	23.726	494.3	
S16	28.2	/	/	22.0	/	/	1287.1	/	/	−12.293	23.786	490.2	
S17	5.8	/	/	5.0	/	/	137.6	/	/	−32.721	1.373	457.7	This study
S18	7.5	/	/	6.4	/	/	203.7	/	/	−32.787	1.317	460.3	
Tycho crater ray by Basilevsky et al. (2018)													
S19	48.7	/	/	39.7	/	/	1355.5	/	/	35.599	−17.319	1623.6	
S20	22.8	/	/	20.2	/	/	808.4	/	/	35.456	−17.309	1620.0	
S21	25.4	/	/	19.6	/	/	992.7	/	/	35.656	−17.301	1625.5	
S22	26.0	/	/	19.9	/	/	794.6	/	/	35.558	−17.157	1624.9	
S23	32.8	/	/	31.6	/	/	1303.6	/	/	35.533	−17.267	1622.7	
S24	41.2	/	/	29.2	/	/	857.5	/	/	35.834	−17.105	1633.0	
S25	27.3	/	/	26.2	/	/	1021.3	/	/	35.593	−17.455	1621.5	
Primary craters in lunar highlands by Bart and Melosh (2007a, 2007b)													
P1	71.6	*69*	3.77	59.7	*54*	10.56	3860.0	*4000*	−3.5	32.689	−0.417	/	V-63-H2
P2	129.8	*410*	−68.34	107.9	*307*	−64.85	17,646.2	*27,400*	−35.60	17.299	2.762	/	V-82-M
P3	39.6	*16*	147.5	37.2	*14*	165.71	938.3	*506*	85.43	−20.434	9.982	/	V-152-H2
P4	56.4	*54*	4.44	48.8	*44*	10.91	790.4	*881*	−10.28	−20.453	10.101	/	V-153-H2
Primary craters in lunar maria by Bart and Melosh (2007a, 2007b)													
P5	12.9	*14*	−7.86	10.8	*12*	−10.0	304.6	*290*	5.034	−44.704	−2.353	/	III-185-H3
P6	30.9	*17*	81.76	24.9	*16*	55.63	661.7	*678*	−2.40	−41.694	1.464	/	III-168-H2
P7	16.3	*16*	1.88	14.6	*13*	12.31	411.9	*229*	79.87	−44.595	−2.364	/	III-186-H3
P8	32.7	*21*	55.71	26.9	*19*	41.58	559.8	*537*	4.246	−44.162	−2.363	/	III-189-H2
P9	155.2	*360*	−56.89	141.2	*332*	−57.47	40,309.8	*41,200*	−2.16	−47.493	23.734	/	V-199-M
P10	24.9	*17*	46.47	17.1	*14*	22.14	494.1	*520*	−4.98	−56.591	13.066	/	V-211-H3
Primary craters in this study													

(*continued on next page*)

Table 1 (*continued*)

Crater ID	Largest boulder (m)			Mean of 5 largest (m)			Crater diameter (m)			Crater center longitude	Crater center latitude	Distance to the primary (km)	Note
	This study	Bart and Melosh (2007a, 2007b)	Difference (%)	This study	Bart and Melosh (2007a, 2007b)	Difference (%)	This study	Bart and Melosh (2007a, 2007b)	Difference (%)				
P11*	81.4	/	/	64.2	/	/	3982.9	/	/	32.697	−0.415	/	This study
P12†	136.5	/	/	124.0	/	/	9260.3	/	/	−100.241	3.311	/	
P13	135.0	/	/	104.6	/	/	9592.1	/	/	−125.689	13.514	/	
P14	13.4	/	/	11.0	/	/	419.9	/	/	−45.033	−1.953	/	
P15	28.8	/	/	27.6	/	/	757.8	/	/	−68.697	39.637	/	
P16	37.2	/	/	32.4	/	/	1371.7	/	/	−70.231	40.793	/	

* Censorinus crater.

† Pierazzo crater.

primary craters were sampled for analysis, which are far more than those sampled by Bart and Melosh (2007a, 2007b). Fig. 1 shows the locations of the selected craters, and their detailed information can be referred to in Table 1.

To delineate and measure the diameter of craters, Bart and Melosh (2007a) used a computer program called "*ImageJ*" (http://rsb.info.nih.gov/ij) and the crater diameters are decided by fitting several 20–30 sided polygons to the rim of the crater. Then the center of those polygons is found with ImageJ and the diameter is gotten by taking the average of the results. This average polygon technique cannot eliminate possible systematic error based on the selection of rim location, although random measurement errors are reduced.

In this study, an ArcGIS tool named "CraterTools" was used in which measurements could be taken independent of map projection (Kneissl et al., 2011). All the craters were determined by three points on the crater rim, and the diameters were automatically measured. This tool can give reliable measurements to the crater diameter in most cases and has been widely used in planetary science community (e.g., Head III et al., 2010; Baker et al., 2011; Fassett et al., 2012; Michael et al., 2012).

2.3. Lunar boulders and measurements

Lunar boulders were first revealed from Ranger photographs in 1965 (Kuiper, 1965), which were individual and intact rock fragments resting on the lunar surface. In images, boulders can be identified as bright pixels on the sunward side of dark pixels (Bart and Melosh, 2007a; Bart and Melosh, 2010) but further careful examination with high resolution is extremely necessary. For example, Küppers et al. (2011) indicated that some features that are either localized accumulations of smaller material (mounds) or rocky outcrops might be mistakenly considered to be boulders. This misrecognition probably depends heavily on the image resolution (e.g., Fig. 6). Thus, a careful examination was carried out in this study to ensure that boulders were correctly identified.

In this study, we adopt the conception that a "boulder" is a positive relief detectable with the presence of an elongated shadow (if the phase angle is greater than 0°) and appears detached from the ground where it stands (Pajola et al., 2018). In addition, a boulder has the diameter of larger than 0.25 m (Neuendorf and Jackson, 2005). Generally, the continuous ejecta, which are composed of massive boulders, cover about 1–2 crater radii around the crater rim, and large boulders tend to be located near the crater rim (Melosh, 1989; Li et al., 2017). Because our study analyzed the relationships between the largest boulders and the crater diameters, the searching area was set to be the concentric annulus between the crater rim and a circle one-crater-radii outward. The top five largest boulders of the craters selected in this study are all within the one-crater-radii distance from the crater rim. On the other hand, to avoid being contaminated by the ejecta from other craters nearby, the area that intersects with other craters and their corresponding search area were excluded (Fig. 2). The excluding area shown in Fig. 2 is the largest of all craters and many craters do not have interrupting craters with boulders in the one-crater-radii range.

In previous boulder measurement, boulders have been considered to be rectangular (Krishna and Kumar, 2016; Li et al., 2017), circular (Di et al., 2016), elliptical (Di et al., 2012; Watkins et al., 2018), ellipsoid (Mazrouei and Ghent, 2017), or directly measured as a line perpendicular to the sun direction (Bart and Melosh, 2007a; Bart and Melosh, 2010). In this research, to make comparison with Bart and Melosh (2007a, 2007b), the length (longest dimension) of a boulder, or the diameter of the boulder in the image, was again determined with the help of "CraterTools". However, in most cases the method of two-point fitting, which measures the length of the boulder independent of projection, was used to determine the boulder size (Fig. 3a). In a few cases, when it was difficult to judge the longest length directly, three-point fitting was used to get the minimum circumcircle of the boulder, and

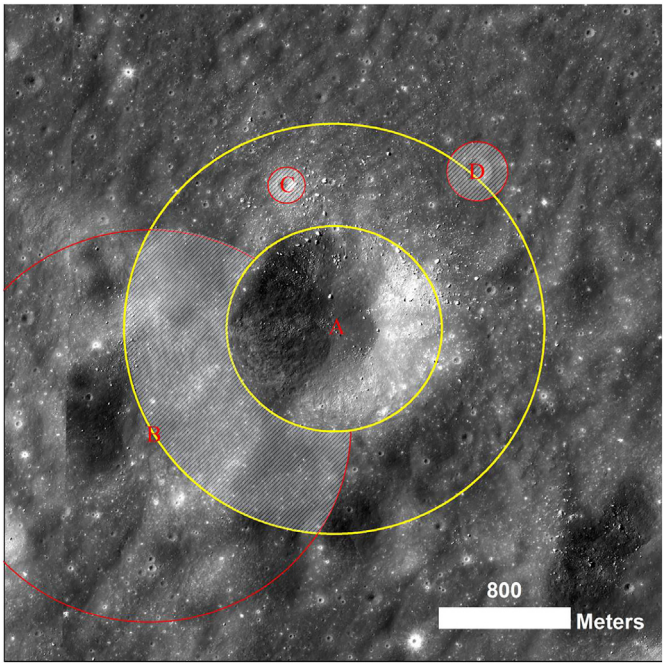

Fig. 2. Schematic diagram of effective boulder search area. The concentric annulus between two yellow circles (initial search area), excluding the intersected parts with other buffered craters B, C, and D (red circles) is defined as the effective boulder search area for crater A. LROC NAC image: m183288763l and m1175168759l. The final effective search area is 2.25 km^2 which takes 61.17% of the initial search area. (For interpretation of the references to colour in this figure legend, the reader is referred to the web version of this article.)

the diameter of the fitted circle was considered to be the length (Fig. 3c). This process can obtain the longest diameter of one boulder. In addition, to minimize the uncertainties from shadows, multiple overlapping NAC images from different illumination conditions were employed, and the largest length from all images was taken as the final boulder size (Fig. 3a compared with Fig. 3b; Fig. 3c compared with Fig. 3d).

3. Results

3.1. Measurements of boulders and craters

Table 1 lists the measurement results of lunar boulders and their corresponding craters, in which the ID of the distant secondary craters begins with an 'S', while the primary craters begin with a 'P'. The size of the largest boulders and the mean of top five largest boulders are both measured. For the distant secondary craters, the size of the largest boulder is 48.7 m, corresponding to a crater diameter of 1355.5 m, which is also the largest crater sampled. Table 1 also includes the locations of the selected craters, giving the distance to the primary craters.

3.2. Relationship between boulders and craters

The relationship between the crater diameter (D) and the largest boulder size (B) is fitted with empirical Eq. (1) (Moore, 1971). In this calculation, we adopted the strategy of using the mean size of the five largest boulders as used by Bart and Melosh (2007a), and the largest boulder size was also used for comparison.

$$B = KD^{2/3} \quad (1)$$

where B and D are in meters, and K is the fitting coefficient (Moore,

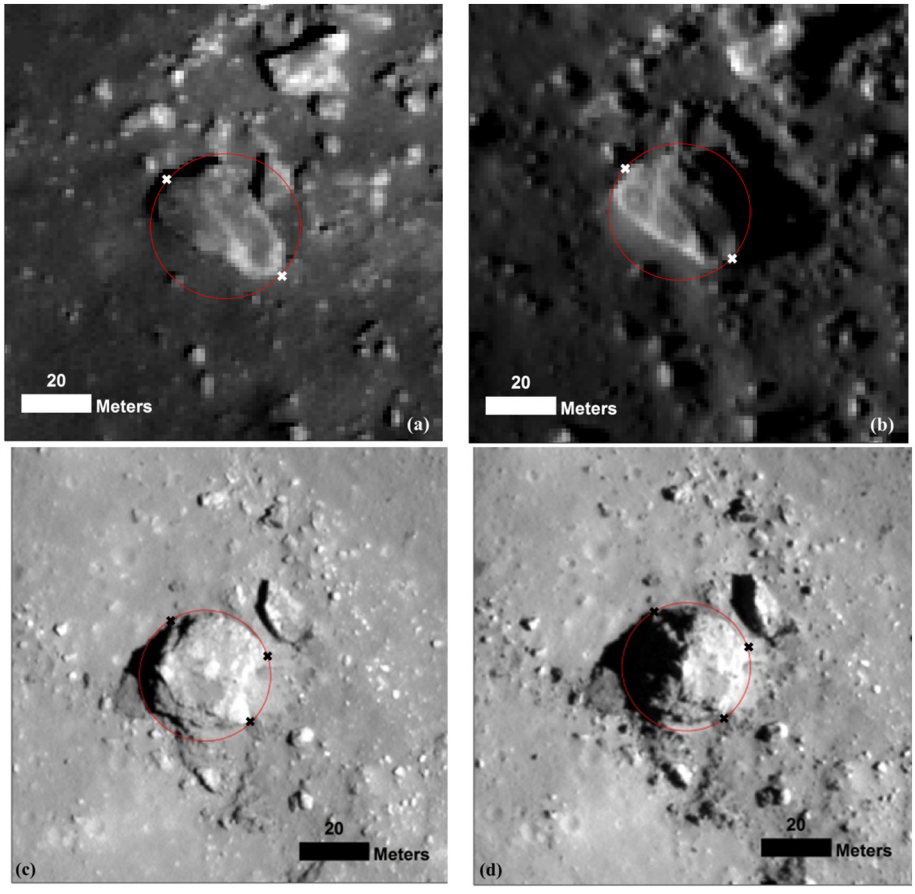

Fig. 3. Schematic diagram of the measurements of the length (longest dimension) of lunar boulders with the help of CraterTools. The locations of the points used to fit the boulders are shown as the crosses. (a) The boulder is fitted by one circle with the method of two points located at the two ends of the longest side of the boulder, which makes the diameter of the circle exactly the length of the boulder, and the measured boulder size is 41.7 m. LROC NAC image: m1150335558l. (b) The same boulder as (a) but from an image with different illumination angles, and the measured boulder size is 39.1 m. LROC NAC image: m181995589l. (c) Three points are used to fit the boulder as one circle because it is difficult to judge the longest dimension directly, and the diameter of the circle is considered as the length of the boulder. The measured boulder size is 37.8 m. LROC NAC image: m159732131re. (d) The same boulder as (c) but from an image with different illumination angles, and the measured boulder size is 36.8 m. LROC NAC image: m159738917re.

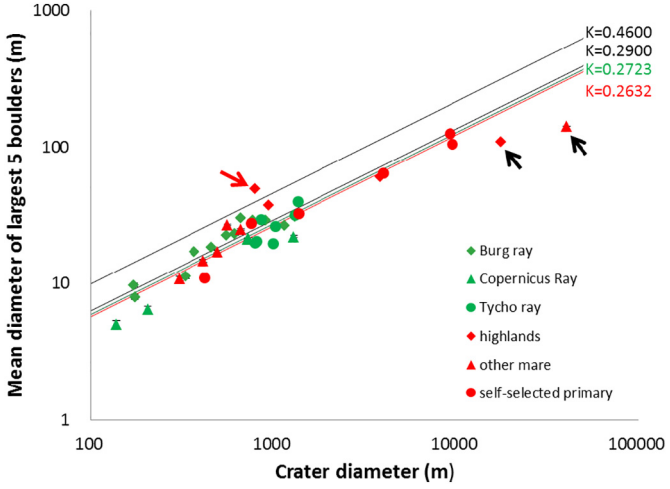

Fig. 4. A log-log plot of the crater diameter versus the mean size of the largest five boulders around the crater. The primary craters are shown in red and secondary craters are displayed in green, while the shapes indicate the groups from Table 1. The red line is the fitted result with Eq. (1) for the primary crater with $K = 0.2632$, and the green line is the result for the secondary crater with $K = 0.2723$ in this study. The two very large craters indicated by the black arrows are not used for fitting because the fitting precision can be heavily damaged ($R^2 = 0.6516$), and when they are excluded, the fitting precision (R^2) can reach 0.9178. The two black lines are the fitted results for the primary crater ($K = 0.29$) and secondary crater ($K = 0.46$) with Bart and Melosh (2007a) for comparison. The crater sample pointed by the red arrow is the only exception (P4 in Table 1) that lies above the fitted line with $K = 0.46$. P4 is within the large crater Copernicus and the formation of the Copernicus crater may have changed the characteristic of the region and make it easier to produce large boulders. (For interpretation of the references to colour in this figure legend, the reader is referred to the web version of this article.)

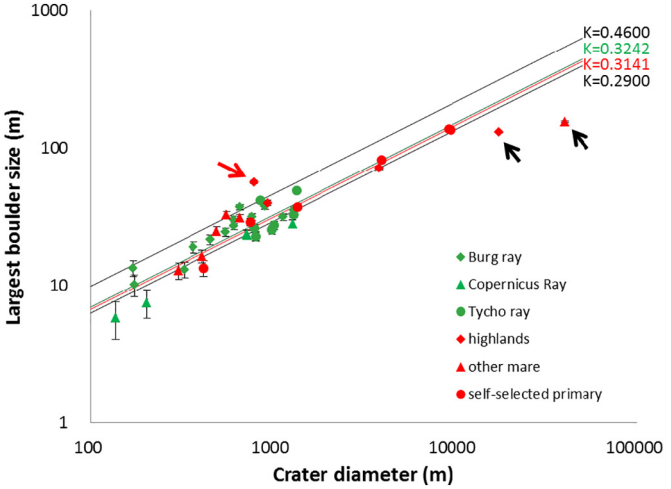

Fig. 5. A log-log plot of the crater diameter versus the largest boulder size around the crater. The primary craters are shown in red, and the secondary craters are displayed in green, while the shapes indicate the groups from Table 1. The red line is the fitted result with Eq. (1) for the primary crater with $K = 0.3141$, and the green line is the result of the secondary crater with $K = 0.3242$ in this study. The two very large craters indicated by the black arrows are also not used for fitting because the fitting precision can be heavily damaged ($R^2 = 0.5902$), and when they are excluded, the fitting precision (R^2) can reach 0.9406. The two black lines are the fitted results of the primary crater ($K = 0.29$) and secondary crater ($K = 0.46$) in Bart and Melosh (2007a) for comparison. The crater sample pointed by the red arrow is the only exception (P4 in Table 1) that lies above the fitted line with $K = 0.46$. (For interpretation of the references to colour in this figure legend, the reader is referred to the web version of this article.)

1971).

Fig. 4 shows the fitted results from Table 1 between the crater diameter and the mean size of the top five largest boulders. All the primary craters are shown in red, while the secondary craters are in green. It is clear that the sizes of the boulders do increase with the diameters of the craters. However, the coefficients between the secondary and primary craters are very close, i.e., the fitted coefficient for primary craters is $K = 0.2632$, and for the secondary craters $K = 0.2723$. Fig. 4 also incorporates the fitted lines with Eq. (1) and the coefficient K = 0.46 for secondary craters, and coefficient K = 0.29 for primary craters, from Bart and Melosh (2007a); all the craters, except one primary crater in the lunar highlands (P4 in Table 1, K = 0.5704), have coefficients smaller than 0.46. In addition, the craters from different groups, i.e., primary craters in lunar highlands, lunar mare (Bart and Melosh, 2007a, 2007b) and selected in this study as well as secondary craters from Burg ray, Copernicus ray and Tycho ray, are indicated by the different shapes in Fig. 4. Fig. 4 shows that the samples from different backgrounds, which means that craters from different target terrains and primary or secondary craters, are mixed in distribution.

The relationship between the crater diameter and the largest boulder size is also analyzed and displayed in Fig. 5. The features and patterns shown in Fig. 5 are very similar to those in Fig. 4, except that the fitted coefficients increase 0.0509 for primary ($K = 0.3141$) and 0.0519 for secondary craters ($K = 0.3242$). Therefore, no matter the largest boulder size or the mean size of the largest five boulders is involved, it seems difficult to distinguish the secondary craters from the primary craters according to the fitted relationships.

Another trend shown in Fig. 4 and Fig. 5 is that the size of the largest boulder increases more slowly when the crater diameter is large enough (e.g., larger than about 17 km in this study), as shown by the two primary craters in the lunar maria and highlands, which have diameter of 17,646.2 m and 40,309.8 m, respectively. The largest crater is a complex crater, while the morphology of the second largest is in the transition from simple to complex as evidenced by the flat floor. The reason for the different trends probably includes: (1) There is a limit for the size of the largest boulders in the lunar surface, regardless of crater diameter; (2) Compared to the simple crater, the diameter of complex crater has been greatly increased in the late stage of crater formation by the gravitational instability (Chapman and McKinnon, 1986; Melosh, 1989).

Except the comparison of the fitted *K*-values between the primary and secondary craters, a statistic analysis of the significance of the *K*-value difference has also been run. The *K*-values of each sample have been calculated by Eq. (1). All the primary and secondary craters are involved including the two largest ones (P2 and P9). The *t*-test method is adopted and the null hypothesis for testing is that there is no significant difference between the *K*-values of the primary and secondary craters. The significance level is set to be $\alpha = 0.05$. The testing results are listed in Table S4, which indicate that $P(T \leq t)$ is ~0.83 when using the largest boulder, and $P(T \leq t)$ is ~0.73 when using the mean size of the top five largest boulders, both of which are larger than 0.05. Besides, the calculated "t Stat" values are smaller than the given critical values. Therefore, the null hypothesis should been accepted that there is no significant difference between the *K*-values of primary and secondary craters no matter the largest boulder size or the mean size of the top five largest boulders is used.

4. Discussion

4.1. Uncertainties in measurements

Crater sizes are determined through three points in the crater rim, and the standard deviation in identifying the rim points can be considered to be a half-pixel, or $\sigma_x = \sigma_y = \sigma =$ ± 0.20 m – ± 1.15 m in this

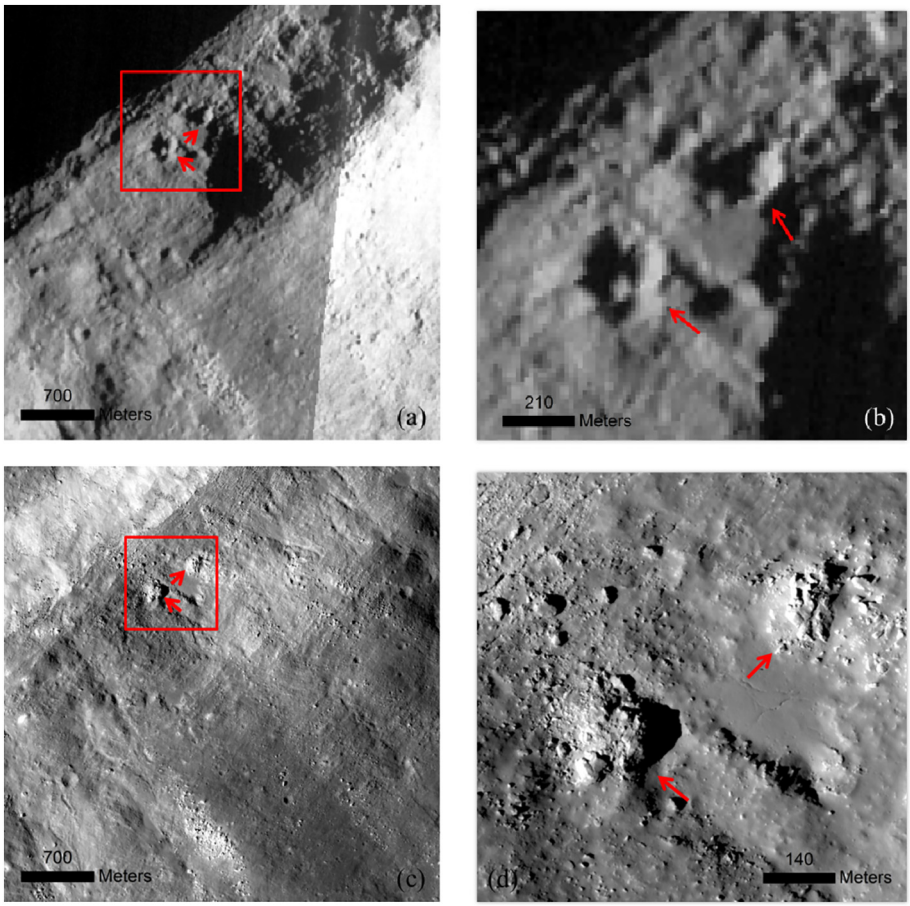

Fig. 6. Boulder identification in a Lunar Orbiter image ((a) and (b), V-199-M) and a LROC NAC image ((c) and (d), m104826902r). Figure (b) and (d) are the zoomed-in views of the features in the red rectangles of (a) and (c), respectively. In the Lunar Orbiter image, two features (arrows) tend to be identified as boulders; however, they are actually a heap of small stones, as seen in the NAC image. (For interpretation of the references to colour in this figure legend, the reader is referred to the web version of this article.)

work. The crater rim is fitted with three points with this uncertainty, and the uncertainties of the crater diameter can be deduced according to conventional error propagation (Ghilani, 2010).

Given three points A, B, and C (they are also used to signify the corresponding angles for triangular ABC), the uncertainty in the diameter of the fit circle is:

$$\sigma_d = \frac{\sqrt{\sin^2 2A + \sin^2 2B + \sin^2 2C}}{2 \sin A \sin B \sin C}\sigma \tag{2}$$

The detailed derivation is trivial, and the results indicate that the uncertainty is only related to the distribution of the selected three points. In this research, the three points delineating the crater rim are generally evenly distributed, as required in CraterTools (Kneissl et al., 2011), which means that the angles of A, B, and C can be considered to be 60°. As a result, $\sigma_d = 1.16$ $\sigma = \pm 0.23$ m – ± 1.33 m.

For the size of the boulders, most of them are measured with two points; that is, the uncertainty is about $\delta_B = 1.41$ $\sigma = \pm 0.28$ m – ± 1.63 m, according to the error propagation law. Considering that the diameters of a few boulders are also derived from circle fitting with three points, the uncertainties of the size of boulders in this research varies from 1.16 σ to 1.41 σ (± 0.23 m – ± 1.63 m).

It can be seen that the absolute error, and thus the derived relative error, is closely related to the image resolution. The absolute error is similar to all the measurements, while the relative error varies especially for boulders. Assuming all measurements are obtained from the lowest resolution images (2.3 m/pixel in this study) and the upper limit of the absolute error (1.63 m) is adopted, the relative error for large boulders, e.g., Crater P9 which has the largest boulder size of 155.2 m, is about 1%. For boulders from small craters, e.g., Crater S17, the largest boulder is 5.8 m, which results in a relative error of 28%.

To illustrate the influence of measurement uncertainties on the fitting results, the error bars have been added to Fig. 4 and Fig. 5. The horizontal and vertical error bars represent crater and boulder measurement uncertainties respectively. For crater measurement, the largest uncertainty (± 1.33 m) is plotted as the horizontal error bars of Fig. 4 and Fig. 5. For single boulder measurement, the largest uncertainty is ± 1.63 m, which is plotted as the vertical error bar in Fig. 5. Since the same boulder measurement method is used and all the boulders are measured by the same person, when assuming that all boulders are digitalized under the lowest image resolution, which is 2.3 m/pixel in this study and caused the largest measurement uncertainties, the resulted boulder sizes should have similar measurement accuracy. For the mean size of the top five largest boulders, the uncertainty can be obtained by the error propagation low (Eq. (3)), and as a result $\delta_{B\_mean} = \pm 0.10$ m $\sim \pm 0.79$ m. Thus, the error bar in Fig. 4 for the boulder measurement is ± 0.79 m. It can be observed that the crater measurement uncertainties have little influence on the crater size, while the boulder measurement uncertainties have relatively larger effect on the small-sized boulders. When the boulder size is larger than ~10 m or the mean size of the five largest boulders is taken, the measurement uncertainties can be also insignificant. Therefore, the existence of measurement uncertainties does not change the result that the secondary and primary craters are difficult to be distinguished by the relationship between crater diameter and boulder size.

$$\delta^2_{B\_mean} = \left(\frac{1}{5}\delta_{B1}\right)^2 + \cdots + \left(\frac{1}{5}\delta_{B5}\right)^2 = \frac{1}{5}\delta^2_B \tag{3}$$

The uncertainty of the coefficient K can be obtained by the uncertainties of boulder and crater size measurement according to the error propagation law. The result is demonstrated in Eq. (4) and it can be seen that the uncertainty of K depends on the crater and boulder size, as well as the image resolution. For the smallest crater in this

research, it has the diameter of 137.6 m and its largest boulder has the size of 5.8 m. As a result, its fitted coefficient K has the uncertainty of ± 0.01 – ± 0.06 within the image resolution range of 0.4 m/pixel – 2.3 m/pixel. For the largest crater with the diameter of 40,309.8 m and largest boulder size of 155.2 m, its fitted uncertainty is $\pm\ 4.0 \times 10^{-4} \sim \pm\ 2.3 \times 10^{-3}$.

$$\delta_K^2 = \left(\frac{K}{B}\right)^2 \delta_B^2 + \left(\frac{2K}{3D}\right)^2 \delta_d^2 = \left(\frac{2.0}{B^2} + \frac{0.59}{D^2}\right) K^2 \sigma^2 \quad (4)$$

4.2. Comparison with previous study

The largest boulder size, mean diameter of the top five largest boulders, crater diameter, and corresponding difference between the measurements from this study and those from Bart and Melosh (2007a, 2007b) are listed in Table 1. For the mean size of the top five largest boulders, the difference varies from −64.85% to 165.71%, in which the negative sign refers to our measured size being smaller than that by Bart and Melosh (2007a, 2007b). The mean difference of the absolute difference is about 37.32%. A similar difference (40.54%) also exists for the size of the largest boulders.

The large discrepancies in boulder size between our measured results and those by Bart and Melosh (2007a, 2007b) may be caused by the differences in boulder recognition, and in this process, the image resolution and illumination conditions have important effects. Fig. 6 is an example that was probably misinterpreted as one boulder in the low-resolution image. In the Lunar Orbiter image V-198-M (Fig. 6a and b), the area encircled by the rectangles looks like a boulder because of the bright pixels on the sunward side of dark pixels (this is also the principle Bart and Melosh (2007a, 2007b) used to identify a boulder); however, in the high-resolution image of LROC NAC (Fig. 6c and d), it is composed of a heap of small stones. The result is a large deviation in the measurement of boulder size. Since Bart and Melosh (2007a, 2007b) did not give the specific location of each boulder involved, the boulders shown in Fig. 6 are just selected by this study to illustrate that the low resolution image can introduce possible interpretation problem.

On the other hand, boulders may be measured to be smaller when the illumination condition is not correctly selected. Fig. 7 shows such an example, in which a boulder was measured to be smaller in size from a Lunar Orbiter image compared with that from a LROC NAC image, since part of the boulder is buried in the shadow. In addition, the deformation of the photographic films from Lunar Orbiter III, V, and Apollo 17 and the scale problem may be another two factors in the measurement uncertainties, which are especially prominent in the measurement of large dimensions, such as the measurement of crater diameter, indicated below.

For the crater diameter, the difference varies from −35.6% to 85.43%, with a mean absolute difference of 18.24%. Crater P2, with a difference of −35.6%, was measured to be 27.40 km in diameter by Bart and Melosh (2007a, 2007b), and this crater was also used by Bart and Melosh (2010) with a measured diameter of 27.422 km. According to Fig. 1F in Bart and Melosh (2010), it can be confirmed that it is the crater Dionysius (Fig. 8). However, the diameter of the crater is 17.25 km, measured by International Astronomical Union (https://planetarynames.wr.usgs.gov/Feature/1542), which is very close to our measurement result of 17.299 km but differs significantly from Bart and Melosh (2007a, 2010). This may be due to the deformation of the photographic films or the scale problem, which can produce different measurements of the crater diameters. Therefore, measurements in this study are much more reliable than previous results.

Except the difference caused by measurement, it seems that the scale problem also exists in Bart and Melosh (2007a, 2007b). Since the Lunar Orbiter III, V, or Apollo 17 images do not have a meaningful m/pixel resolution as that of LROC NAC, the extent of the smallest feature in the image was adopted to represent the resolution in Bart and Melosh (2007a, 2007b), which may cause the scale problem. The boulder-crater size ratios of all the 16 commonly used craters are calculated and the absolute and relative differences between the two studies are shown in Table S1. The relative percentage differences vary from −56.53% to +59.46%. These large percentage differences are more likely to be caused by measurement differences.

The comparison with the results from Krishna and Kumar (2016) can further prove that the measurement in this research is reliable. The Censorinus crater (P11 in Table 1) and the surrounded boulders are involved in both studies. Krishna and Kumar (2016) gave the size of the crater as 3.8 km and the largest length as 78 m (Fig. 7b of their paper). In this study, the crater diameter is 3.98 km and the largest boulder size is 81.4 m, which can be seen in Fig. 9. In Krishna and Kumar (2016), the length of the boulder is measured as the length of the long side of the rectangle fitted to the boundaries, which is similar to the diameter in our research and the measured results are indeed similar between two studies. The residual discrepancy (4.2%) is more likely to be caused by the boulder measurement method difference. The detailed figure about the measurement of the largest boulder of Censorinus crater can be seen in Fig. 9. Both studies used the circle to fit the crater boundary. Therefore, the discrepancy of the crater diameter (2.5%) is more likely to be resulted from the definition of crater rim because the boundary of Censorinus crater is not so regular and circular. The fitted boundary with the three selected rim points in our study is displayed in Fig. 9.

4.3. Relationship analysis between boulders and craters

The two fitted lines for secondary craters and primary craters in Bart and Melosh (2007a) are also plotted in Figs. 4 and 5 as black lines. There is a large difference in the fitted relationships of this study and those in Bart and Melosh (2007a). The fitted line for secondary craters with coefficient $K = 0.46$ is obviously too large compared with the crater samples in this study, and only one crater from the highlands (Crater P4, $K = 0.5704$) lies above this line. This crater is located in the Copernicus crater and this region contains many rich-in-boulder features. The other crater (P3) with large fitting coefficient ($K = 0.3878$) also lies in the vicinity. It may be that the previous impacting event to produce the Copernicus crater changed the characteristic of the region and made it easier to produce large boulders. The large difference between our results and those of Bart and Melosh (2007a) are not only caused by the inconsistency in the measurements, but also because the different number of crater samples involved in two studies. In addition, our results of $K = 0.2632$ (mean size of top five largest boulders) and $K = 0.3141$ (largest boulder) for primary craters, and $K = 0.2723$ (mean size of top five largest boulders) and $K = 0.3242$ (largest boulder) for secondary craters are in the range of $K = 0.11 – 0.32$ given by Moore (1971).

The top two largest sampled craters, as indicated in Fig. 4 and Fig. 5, are not used for the above fitting, as described in Section 3.2. When the two sampled craters are incorporated, the fitted coefficients (K) for primary craters are 0.1619 for the mean size of the top five largest boulders and 0.1875 for the largest boulders. However, the fitting precision decreases significantly, as we have explained, probably due to the upper limit of the largest boulder size in the lunar surface and they are complex craters instead of simple craters. Because the diameter of the complex crater has greatly increased in the modification stage mainly caused by the gravity (Melosh, 1989, Chapter 8), it is reasonable to exclude them in fitting as we have done in section 3.2.

Generally, our results indicate that the fitted coefficients for primary and secondary craters have a very small difference (~5%), and many secondary craters have largest boulders that are of similar size to the primary craters, given that their diameters are also similar. The results demonstrate that the principle to distinguish distant secondary craters from primary craters proposed by Bart and Melosh (2007a) may be impractical, which is discouraging.

Bart and Melosh (2007a) had explained that boulder size is largely a function of the stress gradient in the target rock. Higher shock pressure

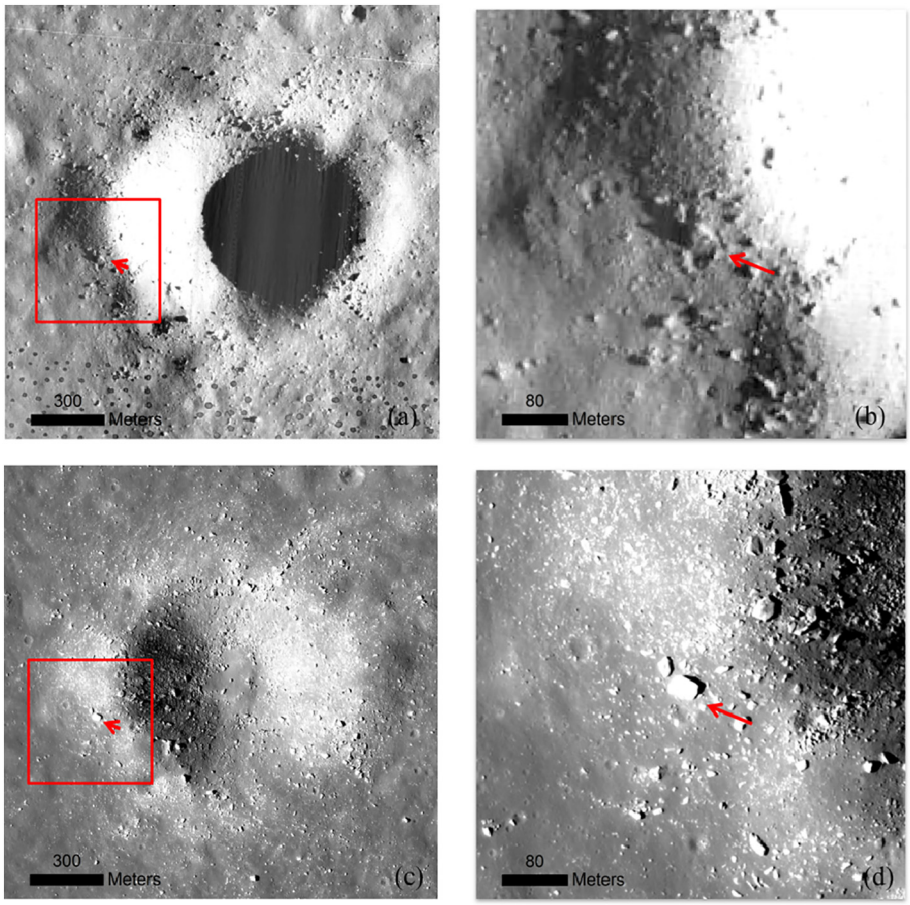

Fig. 7. Boulders from the Lunar Orbiter image ((a) and (b), V-152-H2) are measured to be smaller than those from the LROC NAC image ((c) and (d), m1175545925l) due to the influence of unsatisfactory illumination. In the Lunar Orbiter image, the low incidence angle caused a relief shadow in which part of boulder was buried. Figure (b) and (d) are the zoomed-in views of the features in the red rectangles of (a) and (c), respectively. (For interpretation of the references to colour in this figure legend, the reader is referred to the web version of this article.)

caused by higher impact velocity tends to generate larger stress gradients and then produce smaller boulders for a given crater size (Bart and Melosh, 2007a). However, it is probably the stress gradient after attenuation over a long distance, instead of around the impact center, that is responsible for the formation of the largest boulders. After the shock wave was sufficiently attenuated, the stress gradient should be very different to that around the impact center. This can be proven by the fact that most of the large boulders are distributed around crater rims, where the shock wave has been substantially attenuated such that the ejection velocity declines to almost zero (Melosh, 1989). If it is the case, the target properties may be much more important than the initial stress gradient. So the relationships between the diameter of largest boulder and the crater are similar for primary and secondary craters. This problem deserves further study in future through other methods, e.g., laboratory tests and numerical simulations.

5. Conclusion

In this study, the relationship between the crater diameter and the largest boulder size, which has been proposed as a method to distinguish secondary craters from primary craters by Bart and Melosh (2007a), is reanalyzed using 41 sampled craters with high-resolution LROC NAC images. The results indicate that the crater diameter and the largest boulder size do have an exponential relationship: $B = KD^{2/3}$. However, the coefficient K in this relationship has a very small difference (~5%) between primary and secondary craters, which makes it an

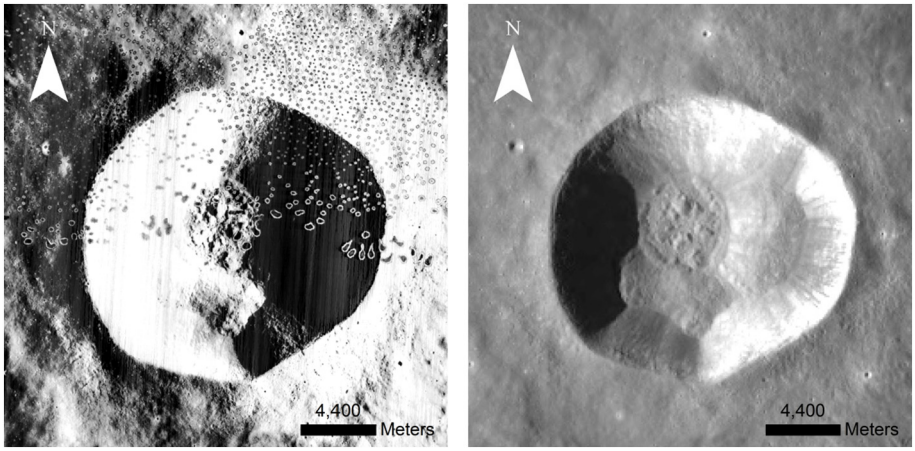

Fig. 8. Crater Dionysius from Lunar Orbiter image V-82-M (left) and LROC WAC mosaic (right). The crater was measured to be 27.40 km in diameter by Bart and Melosh (2007a, 2007b), and this crater was also used by Bart and Melosh (2010) with a measured diameter of 27.422 km. However, the diameter of the crater is 17.25 km, as measured by the International Astronomical Union (https://planetarynames.wr.usgs.gov/Feature/1542), which is very close to our measurement result of 17.299 km.

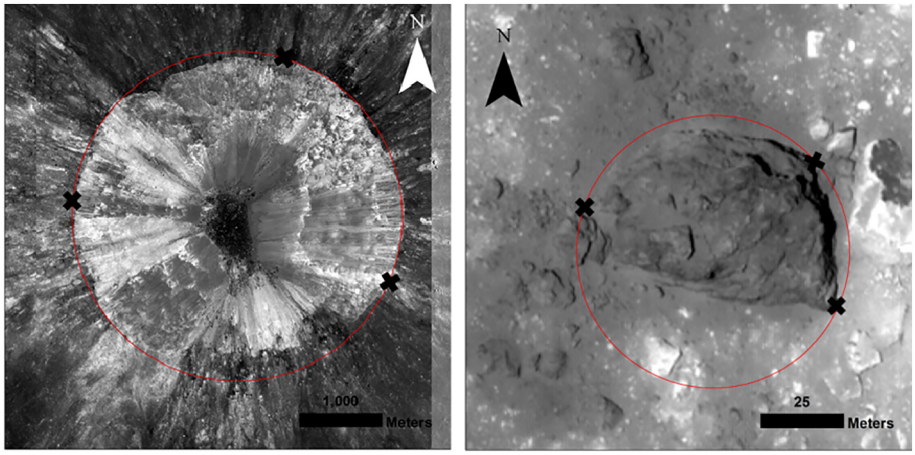

Fig. 9. Censorinus crater and its largest boulder with the fitted boundaries (LROC NAC image: m139694087l, m139694087r and m159732131l). The three points used to define the boundary are shown as crosses.

unreliable discriminator for primary and secondary craters, contrary to that proposed by Bart and Melosh (2007a). Further effort, e.g., research about the boulder size distribution around a crater, is necessary to create a reliable criterion for this important problem.

Acknowledgements

The authors gratefully acknowledge Arizona State University for providing LROC NAC images. The authors also thank Thomas Kneissl for the software CraterTools. This work was supported by the Key Research Program of the Chinese Academy of Sciences (Grant no. XDPB11), National Natural Science Foundation of China (Grant no. 41490635 and 41590851) and Science and Technology Development Fund of Macau (Macau FDCT grant No. 131/2017/A3).

Appendix A. Supplementary data

Supplementary data to this article can be found online at https://doi.org/10.1016/j.icarus.2019.05.009.

References

Ahrens, T.J., O'Keefe, J.D., 1978. Energy and mass distributions of impact ejecta blankets on the moon and Mercury. In: The 9th Lunar and Planetary Science Conference Proceedings, pp. 3787–3802.
Anderson, J.A., Sides, S.C., Soltesz, D.L., et al., 2014. Modernization of the integrated software for imagers and spectrometers. In: Lunar and Planetary Science Conference, pp. 2039.
Baker, D.M.H., Head, J.W., Schon, S.C., Ernst, C.M., Prockter, L.M., Murchie, S.L., Denevi, B.W., Solomon, S.C., Strom, R.G., 2011. The transition from complex crater to peak-ring basin on Mercury: new observations from MESSENGER flyby data and constraints on basin formation models. Planet. Space Sci. 59 (15), 1932–1948.
Bart, G.D., Melosh, H.J., 2007a. Using lunar boulders to distinguish primary from distant secondary impact craters. Geophys. Res. Lett. 34, L07203.
Bart, G.D., Melosh, H.J., 2007b. Correction to "using lunar boulders to distinguish primary from distant secondary impact craters". Geophys. Res. Lett. 34, L10203.
Bart, G.D., Melosh, H.J., 2010. Distributions of boulders ejected from lunar craters. Icarus 209, 337–357.
Basilevsky, A.T., Michael, G.G., Kozlova, N.A., 2018. Rock spatial densities on the rims of the Tycho secondary craters in Mare Nectaris. Planet. Space Sci. 153, 120–126.
Chapman, C.R., McKinnon, W.B., 1986. Cratering of planetary satellites. In: Burns, J.A., Matthews, M.S. (Eds.), Satellites, pp. 492–580.
Di, K., Yue, Z., Liu, Z., Wang, S., 2012. Automated rock detection and shape analysis from Mars rover imagery and 3D point cloud data. J. Earth Sci. 24 (1), 125–135.
Di, K., Xu, B., Peng, M., et al., 2016. Rock size-frequency distribution analysis at the Chang'E-3 landing site. Planet. Space Sci. 120, 103–112.
Fassett, C.I., Thomson, B.J., 2014. Crater degradation on the lunar maria: topographic diffusion and the rate of erosion on the Moon. J. Geophys. Res. Planets 119. https://doi.org/10.1002/2014JE004698.
Fassett, C.I., Head, J.W., Kadish, S.J., Mazarico, E., Neumann, G.A., Smith, D.E., Zuber, M.T., 2012. Lunar impact basins: stratigraphy, sequence and ages from superposed impact crater populations measured from lunar orbiter laser altimeter (LOLA) data. J. Geophys. Res. 117, E00H06.
Ghilani, C.D., 2010. Adjustment Computations: Spatial Data Analysis. John Wiley & Sons, Incorporation, New Jersey, pp. 86–91.
Head III, J.W., Fassett, C.I., Kadish, S.J., Smith, D.E., Zuber, M.T., Neumann, G.A., Mazarico, E., 2010. Global distribution of large lunar craters: implications for resurfacing and impactor populations. Science 329, 1504–1507.
Head, J.N., Melosh, H.J., Ivanov, B.A., 2002. Martian meteorite launch: high-speed ejecta from small craters. Science 298 (5599), 1752–1756.
Hiesinger, H., van der Bogert, C.H., Pasckert, J.H., et al., 2012. How old are young lunar craters? J. Geophys. Res. Planets 117 (E12), 1–15.
Kneissl, T., Gasselt, S., Neukum, G., 2011. Map-projection-independent crater size-frequency determination in GIS environments—new software tool for ArcGIS. Planet. Space Sci. 59 (11), 1243–1254.
Krishna, N., Kumar, P.S., 2016. Impact spallation processes on the moon: a case study from the size and shape analysis of ejecta boulders and secondary craters of Censorinus crater. Icarus 264, 274–299.
Kuiper, G.P., 1965. The surface structure of the moon. In: The Nature of the Lunar Surface. The Johns Hopkins Press, Baltimore, pp. 99–105.
Kumar, P.S., Kumar, A.S., Keerthi, V., et al., 2011. Chandrayaan-1 observation of distant secondary craters of Copernicus exhibiting central mound morphology: evidence for low velocity clustered impacts on the Moon. Planet. Space Sci. 59 (9), 870–879.
Küppers, M., Moissl, R., Vincent, J.B., et al., 2011. Boulders on Lutetia. Planet. Space Sci. 66 (1), 71–78.
Li, Y., Basilevsky, A.T., Xie, M., et al., 2017. Correlations between ejecta boulder spatial density of small lunar craters and the crater age. Planet. Space Sci. https://doi.org/10.1016/j.pss.2017.08.007. in press.
Mazrouei, S., Ghent, R.R., 2017. Towards an understanding of initial crater rock populations: Boulder distribution around Copernicus crater. In: 48th Lunar and Planetary Science Conference, (Abstract #2507).
McEwen, A.S., 2018. Luminous Pierazzo crater. Lunar Reconnaissance Orbiter Camera. Arizona State Universityhttp://lroc.sese.asu.edu/posts/1000.
McEwen, A.S., Bierhaus, E.B., 2006. The importance of secondary cratering to age constraints on planetary surfaces. Annu. Rev. Earth Planet. Sci. 34 (1), 540–567.
Melosh, H.J., 1989. Impact Cratering: A Geologic Process. Oxford University Press, New York.
Michael, G.G., Platz, T., Kneissl, T., Schmedemann, N., 2012. Planetary surface dating from crater size–frequency distribution measurements: spatial randomness and clustering. Icarus 218, 169–177.
Michael, G.G., Kneissl, T., Neesemann, A., 2016. Planetary surface dating from crater size-frequency distribution measurements: Poisson timing analysis. Icarus 277, 279–285.
Moore, H.J., 1971. Large blocks around lunar craters, in analysis of Apollo 10 photography and visual observations. NASA Special Publication 232, 26–27.
NAIF, 2014. Lunar Reconnaissance Orbiter Camera (LROC) Instrument Kernel v18. http://naif.jpl.nasa.gov/pub/naif/pds/data/lro-l-spice-6-v1.0/lrosp_1000.
Neuendorf, K.K.E., Mehl, Jr. J.P., Jackson, J.A. (Eds.), 2005. Glossary of Geology (5th edition). Alexandria, Virginia: American Geological Institute, 79.
Oberbeck, V.R., Morrison, R.H., 1973. On the formation of the lunar herringbone pattern. In: Processing Lunar Planetary Science Conference. vol. 4. pp. 107–123.
Orgel, C., Michael, G., Fassett, C.I., et al., 2018. Ancient bombardment of the inner solar system: reinvestigation of the "fingerprints" of different impactor populations on the lunar surface. J. Geophys. Res. 123, 748–762.
Pajola, M., Pozzobon, R., Lucchetti, A., et al., 2018. Abundance and size-frequency distribution of boulders in Linné crater's ejecta (Moon). Planet. Space Sci. https://doi.org/10.1016/j.pss.2018.11.008. in press.
Robinson, M.S., Brylow, S.M., Tschimmel, M., et al., 2010. Lunar reconnaissance orbiter camera (LROC) instrument overview. Space Sci. Rev. 150 (1–4), 81–124.
Sato, H., Robinson, M.S., Hapke, B., Denevi, B.W., Boyd, A.K., 2014. Resolved Hapke parameter maps of the moon. J. Geophys. Res. Planets 119, 1775–1805.
Shoemaker, E.M., Hackman, R.J., Eggleton, R.E., 1962. Interplanetary correlation of geologic time. Adv. Astronaut. Sci. 8, 70–79.
Speyerer, E.J., Robinson, M.S., Denevi, B.W., the LROC Science Team, 2011. Lunar

Reconnaissance Orbiter Camera Global Morphological Map of the Moon, Lunar Planetary Science Conference. (Abstract #2387).
van der Bogert, C.H., Hiesinger, H., McEwen, A.S., et al., 2010. Discrepancies between crater size-frequency distributions on ejecta and impact melt pools at lunar craters: an effect of differing target properties? In: 41th Lunar and Planetary Science Conference, (Abstract #2165).
Wagner, R.V., Speyerer, E.J., Robinson, M.S., LROC Team, 2015. New mosaicked data products from the LROC team. In: 46th Lunar and Planetary Science Conference, (Abstract #1473).
Watkins, R.N., Mistick, K., Jolliff, B.L., et al., 2018. Boulder distributions around young lunar impact craters: case study of South Ray Crater. In: 49th Lunar and Planetary Science Conference, (Abstract #1201).
Wilcox, B.B., Robinson, M.S., Thomas, P.C., Hawke, B.R., 2005. Constraints on the depth and variability of the lunar regolith. Meteorit. Planet. Sci. 40, 695–710.
Wilhelms, D.E., Oberbeck, V.R., Aggarwal, H.R., 1978. Size-frequency distributions of primary and secondary lunar impact craters. In: The 9th Proceedings of the Lunar Planetary Science Conference, pp. 3735–3762.